# Atomic Structural Catalogue of Defects and Vertical Stacking in 2H/3R Mixed Polytype Multilayer $WS_2$ Pyramids

*Gyeong Hee Ryu[1], Jun Chen[1], Yi Wen[1], Si Zhou[1], Ren-Jie Chang[1], and Jamie H. Warner[1]**

[1] Department of Materials, University of Oxford, 16 Parks Road, Oxford OX1 3PH, United Kingdom

*Email: Jamie.warner@materials.ox.ac.uk

ABSTRACT. We examine the atomic structure of chemical vapour deposition grown multilayer $WS_2$ pyramids using aberration corrected annular dark field scanning transmission electron microscopy coupled with an in-situ heating holder. The stacking orders and specific types of defects after partial degradation by S and W atomic loss at high temperature are resolved layer-by-layer. Our study of an individual $WS_2$ pyramid with at least six layers, reveals a mixed 2H and 3R polytype stacking. Etching occurred both top and bottom of the $WS_2$ pyramid, which aids in determining the exact vertical layer stacking configurations in the thicker regions. We provide an extensive catalogue of the contrast profiles associated with defects in $WS_2$ as a function of layer number and stacking type, as imaged using ADF-STEM. These results provide extensive details about the identification of a wide range of defects in $S_2$

layers, and the unique ADF-STEM contrast patterns that arise from complex multilayer stacking.

KEYWORDS. Pyramid, Multilayer $WS_2$, stacking order, TMDs, STEM

Transition-metal dichalcogenides (TMDs) have a variety of phases depending on intralayer stacking orders and there are 1H, 1T, and 1T’ phases which each have different electrical properties.[1-3] In monolayer TMDs, 1H and 1T phases consist of three atomic planes, which top and bottom planes being chalcogen atom with sandwiched metal atom plane sharing the same planar symmetry.[3-4] The intralayer stacking order in 1H and 1T takes ABA and ABC stacking sequences, respectively. 1T phase is dynamically unstable so it undergoes a distortion to reduce the dimensionally of the 2D system into three equivalent 1D zigzag chains, giving rise to the so-called distorted 1T phase (1T’).[5-7] Even though there are various polytypes, bare flakes and synthesized TMDs have been reported as the 1H phase, such as 2H and 3R (Figure 1f), which follows the AA′, AB sequences, respectively,[3-4] because 1T and 1T’ stacked materials have poor stabilities.[8-9]

Regarding TMDs, atomic defects can be formed for various reasons. For example, they can be formed while the materials are synthesized, aged, and heated. Besides, when we analyze the materials using transmission electron microscopy, they are also able to be induced by the electron beam. The detailed atomic structure of the defects until bilayer TMDs has been studied by annular dark-field scanning transmission electron microscopy (ADF-STEM)[10-13] but induced defects formed by electron beam irradiation or heating in monolayer and bilayer TMDs are rapidly expanded, deformed and absorbed due to their fast diffusion rate.[14-19] However, the dynamics of defects in multilayer materials are not fast compared to less than the bilayer TMDs because the upper and lower layers act as protective layers[20-21] so their diffusion rate naturally slows down and there are some limits to forming new induced defects except for intrinsic defects.[22] In addition, as the number of layers of the materials increases, it is not easy to quantify the exact stacking sequence, structure, and location of the defects. On the other hand, if we keep track of the step edge arrangements of materials from the bottom up one by one using the ADF-STEM, stacking sequences and atomic structures of defects can be confirmed. ADF-STEM is powerful for structural studies of TMDs such as $WS_2$ as this reveals Z-atom information in the contrast of its images.[23-24] Furthermore, once the position of the structural defect is understood, the etching direction and aging tendency of the material can be figured out. Directly grown bilayer TMDs sheets are considered to have 2H or 3R stacking sequences[25-28], but the specific study on the stacking orders and intrinsic defects above more than the trilayer have not been reported in detail.

Here we examine the stacking sequence and the atomic structure of the defects in multilayer $WS_2$ pyramids synthesized by CVD using aberration-corrected ADF-STEM imaging and multislice image simulation. An in-situ heating holder is used to raise the temperature of the sample up to 1000°C within the TEM, close to the melting point, to promote atomic loss and the partial etching of the sample. Then we cooled back to 700°C for imaging of the thermal degraded structure. We confirm the stacking order up to a pentalayer by keeping track of the step edge configuration of the $WS_2$ domain above the larger $WS_2$ supporting monolayer and then find out where the pores and defects exist and which atoms should be missed to match the defects seen in the ADF-STEM images. A detailed atomic structural catalogue of ADF-STEM contrast as a function of layer number and defect type is then summarized. And, we analyze the combined 2H and 3R stacked quadralayer and pentalayer. The atomic configurations on the multilayers and some left layers after partially etched are particularly periodic about the 1H phase. This study can be applied to all TMDs materials with 1H phase, and the image of the existing defects can sufficiently infer the atomic structure.

## Results and Discussion

Figure 1a shows an ADF-STEM image of multilayer $WS_2$ pyramids having 1H phase and Figure 1b shows a schematic of the $WS_2$ pyramid. The samples were partially degraded after heating to 1000ºC in-situ within the TEM using a heating holder. But upon cooling to 700ºC, the sample was stable and then imaged. The contrast of the ADF-STEM image is displayed according to the number of layers, so the number of layers can be found out (Figure 1c). Figure 1d indicates an intensity line profile measured from a red arrow in Figure 1c which represents this multilayer is pyramid-shaped. By tracing the layers from the lower layer to the top layer (Figure 1c-g), stacking orders can be figured out, such as 2H and 3R depending on how the interlayer are stacked such as AA' and ABC sequences, respectively (Figure S1). 2H stacked $WS_2$ shows that the W (S) atoms in one layer overlap with the S (W) atoms in the other layer. The lattice orientation between the two layers is rotated by 60° with all atoms in the two layers fully eclipsed. While 3R stacked $WS_2$ shows that double stacked S atoms in one layer are located above (below) the centres of the hexagonal rings in the other layer. In this configuration, three different atomic columns are observed in the top down projection; a single W atom, two S atoms plus one W atom, and two S atoms, respectively. As a side note, this 3R stacking can be considered such as AB-1 and AB-2 as shown in Figure S1b. If one layer shifts along the red arrow, it would be AB-1 stacking, where W atoms in the top-layer (T-L) overlap with S atoms in the bottom-r (B-L). For AB-2 stacking, if one layer shifts along the blue arrow, S atoms in T-L overlap with W atoms in B-L.

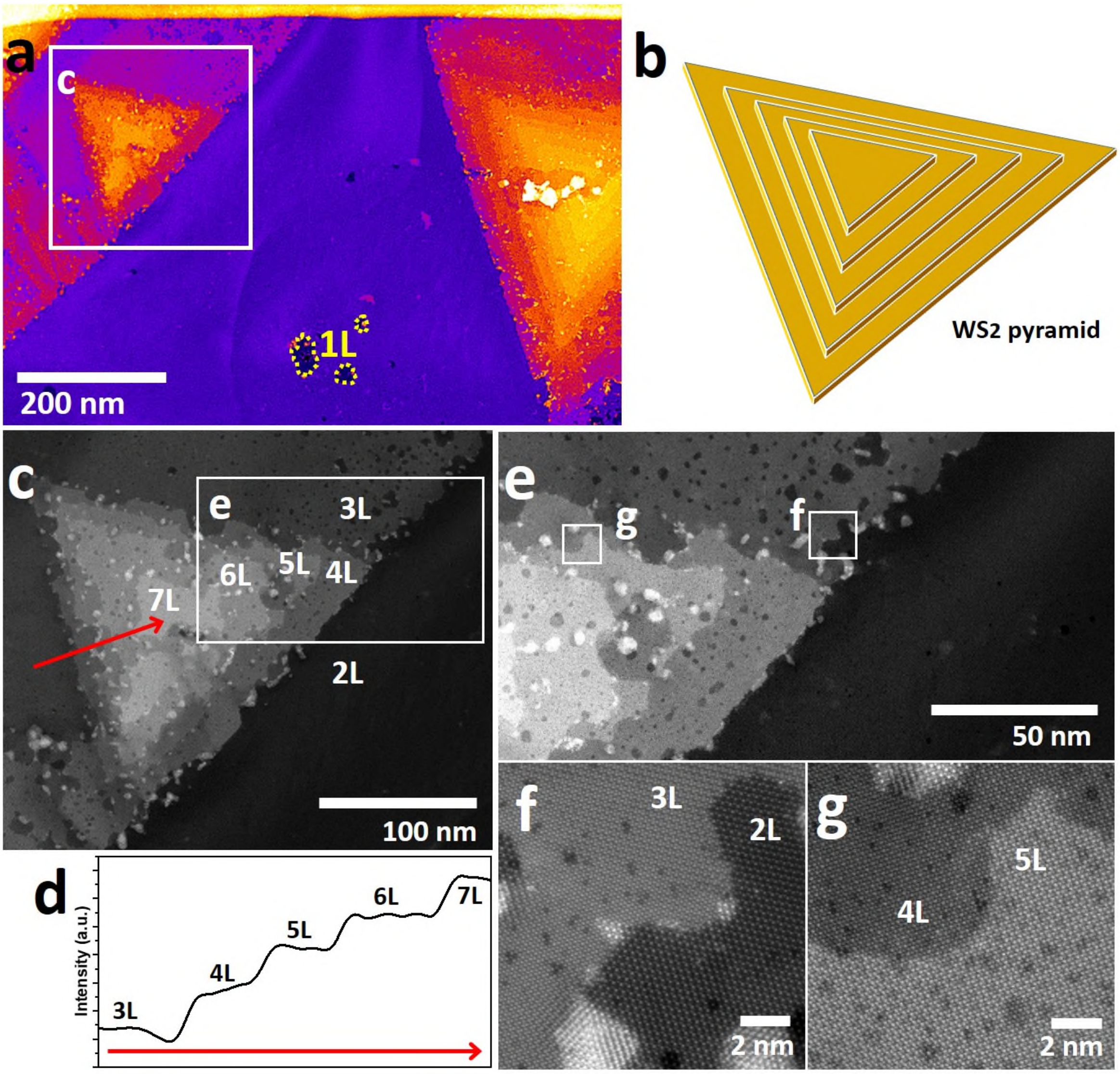

**Figure 1.** (a) Low magnification ADF-STEM image showing synthesized multilayer $WS_2$ pyramids. (b) Schematic of a multilayer $WS_2$ pyramid. (c) Magnified image from the white box in (a). (d) Intensity line profile measured from the red arrow in (c) showing the number of layers. (e) Magnified image from the white box in (c). (f, g) Magnified images of step edge configurations between the lower layer and the layer just above it from the white boxes in (e), respectively.

Figure 2a and b show the multilayer $WS_2$ pyramid and a magnified image, indicated by a white box in Figure 2a, showing a step edge configuration of trilayer $WS_2$. Bilayer (2L) and trilayer (3L) each have an obvious contrast difference as the contrast comes from the atom packing information along the Z-axis of the stacking order in bi- and trilayer $WS_2$. Figure 2c shows a magnified image taken from the region marked with a white box in Figure 2b. Figure 2d shows a multislice ADF image simulation corresponding to an atomic model in Figure 2e. Figure 2f shows a side view of the atomic model in Figure 2e. Intensity line profiles across two adjacent lines through the trilayer $WS_2$ step edge, labelled by 1 and 2 in Figure 2c and d, are measured for both experimental and simulated ADF images, showing good agreements (Figure 2g and h). The ADF-STEM image indicates that this trilayer region exhibits 3R (ABC) stacking and this bilayer region exhibits 3R (AB-2) stacking. About the 3R stacked trilayer, all contrast of the columns comes from overlapped W and $S_2$ so, if there are no any defects, the contrast would be even but some residual C contaminations could have effects on the contrast.

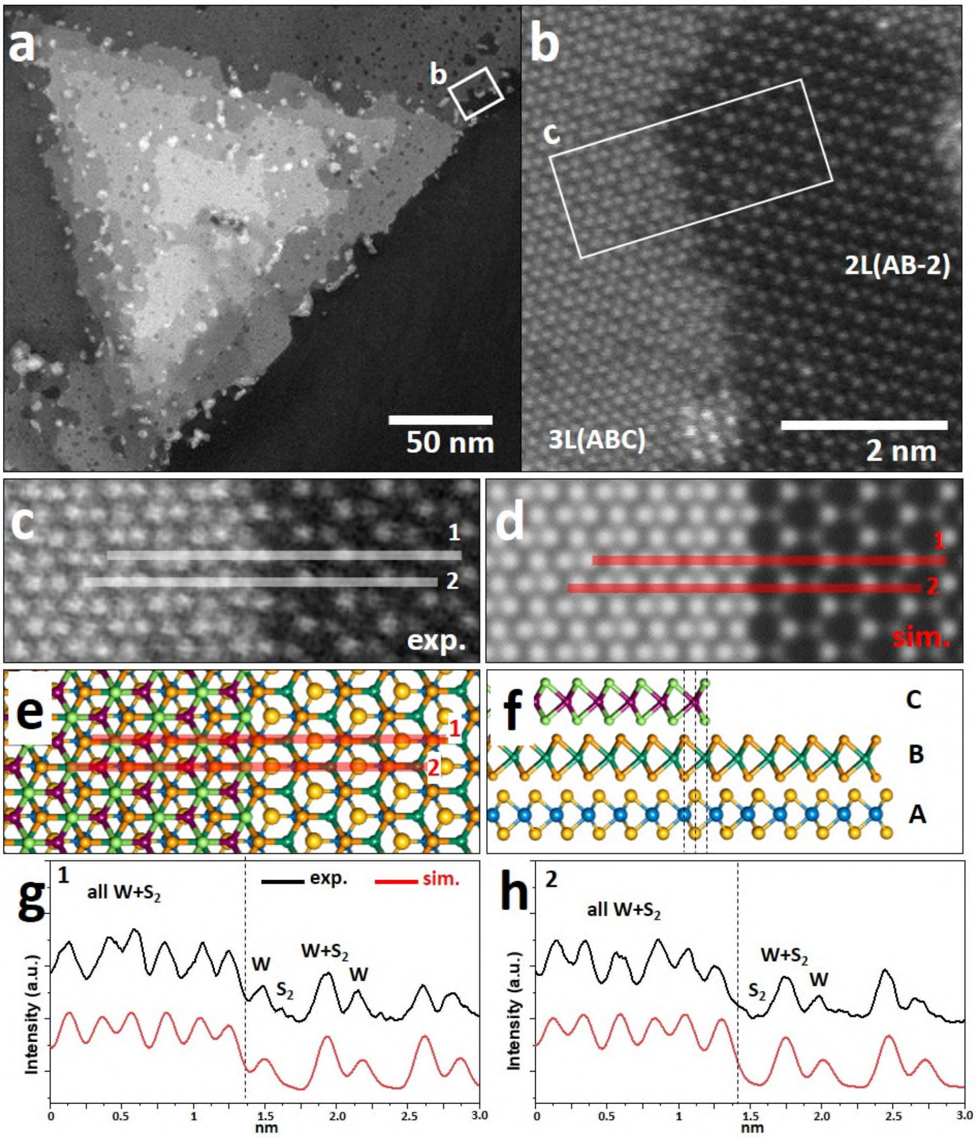

**Figure 2.** (a) ADF-STEM image showing the multilayer $WS_2$ pyramid. (b) Magnified image from the white box in (a) showing the step edge configuration of 3R (ABC) stacked trilayer $WS_2$. (c) Magnified image of the white box in (b). (d) Multislice ADF-STEM image simulation corresponding to the atomic model in (e). (e) Atomic model based on (c). (f) Side view of (e). (g) Intensity line profiles measured from the white and red lines labelled 1 in (c) and (d). (h) Intensity line profiles measured from the white and red lines labelled 2 in (c) and (d).

Figure 3a shows some nanopores which exist in the 3R stacked trilayer $WS_2$. This trilayer can also have a variety of types of nanopores but there are two possibilities to explain the atomic structure about some pores (see Figure S2 and S3) because we have to consider which layer atoms are preferentially missed. Figure 3b indicates a magnified image of a white box labelled by b in Figure 3a. Figure 3c and d show multislice ADF-STEM image simulations corresponding to atomic models in Figure S4a and b which structures are 1 S pair is missed in A ($V_{S2}$ in A) and C ($V_{S2}$ in C), respectively. ADF-STEM imaging is projected images so the number of same kinds of packed atoms visualizes as same contrast regardless of stacking order. So, in the 3R stacked trilayer, it could not confirm that which layer has defects in the case of some types but they can be observed at any layer because most defects described in this study are overlapped defects of each layer with atom ejections except some cases such as Figure 3(c) and (d). If they are engineered defects by electron beam irradiation, atom ejections occur sequentially from the bottom layer. Figure 3e shows an intensity line profile measured from a white line in Figure 3b has good agreements with intensity line profiles measured from red and blue lines in Figure 3c and d. Figure 3f is a magnified image of a white box labelled by f in Figure 3a. Figure 3g and h show multislice ADF-STEM image simulations corresponding to atomic models in Figure S4c and d which structures are 3 S pairs are missed in A and 1 S atom is missed in C ($V_{3S2}$ in A/$V_S$ in C, Figure S4c) and 1 S atom is missed in B and 3 S pairs are missed in C ($V_S$ in B/$V_{3S2}$ in C, Figure S4d), respectively. Figure 3i shows an intensity line profile measured from a white line in Figure 3f has a good agreement with intensity line profiles measured from red and blue lines in Figure 3g and h. Figure 3j is a magnified image of a white box labelled by j in Figure 3a. Figure 3k and l show multislice ADF-STEM image simulations corresponding to atomic models in Figure S4e and f. The atomic structure of Figure 3k is 1 S atom is missed in A, another 1 S atom is missed in B, and 2 S pairs are missed in C ($V_S$ in A/$V_S$ in B/$V_{2S2}$ in C, Figure S4e). The atomic structure of Figure 3l is that 2 S pairs are missed in A, 1 S atom is missed in B, and another 1 S atom is missed in C ($V_{2S2}$ in A/$V_S$ in B/$V_S$ in C, Figure S4f). They both have the same number of the packed atoms along the Z-axis but, in the case of Figure 3l, the S vacancy existing in B, indicated by a black-circle line in Figure S4(f), can be protected by A and C. Therefore, the structure of Figure 3k could be reasonable unless an intrinsic S vacancy exists in B in advance. Figure 3m shows an intensity line profile measured from a white line in Figure 3j has a good agreement with intensity line profiles measured from red and blue lines in Figure 3k and l. Figure 3n is a magnified image of a white box labelled by n in Figure 3a. Figure 3o shows a multislice ADF-STEM image simulation corresponding to an atomic model in Figure S4g. This atomic structure is 2 S pairs are missed in A and 1 S pair is missed in C ($V_{2S2}$ in A/$V_{S2}$ in C, Figure S4g). Figure 3p shows an intensity line profile measured from a white line in Figure 3n has a good agreement with an intensity line profile measured from a red line in Figure 3o.

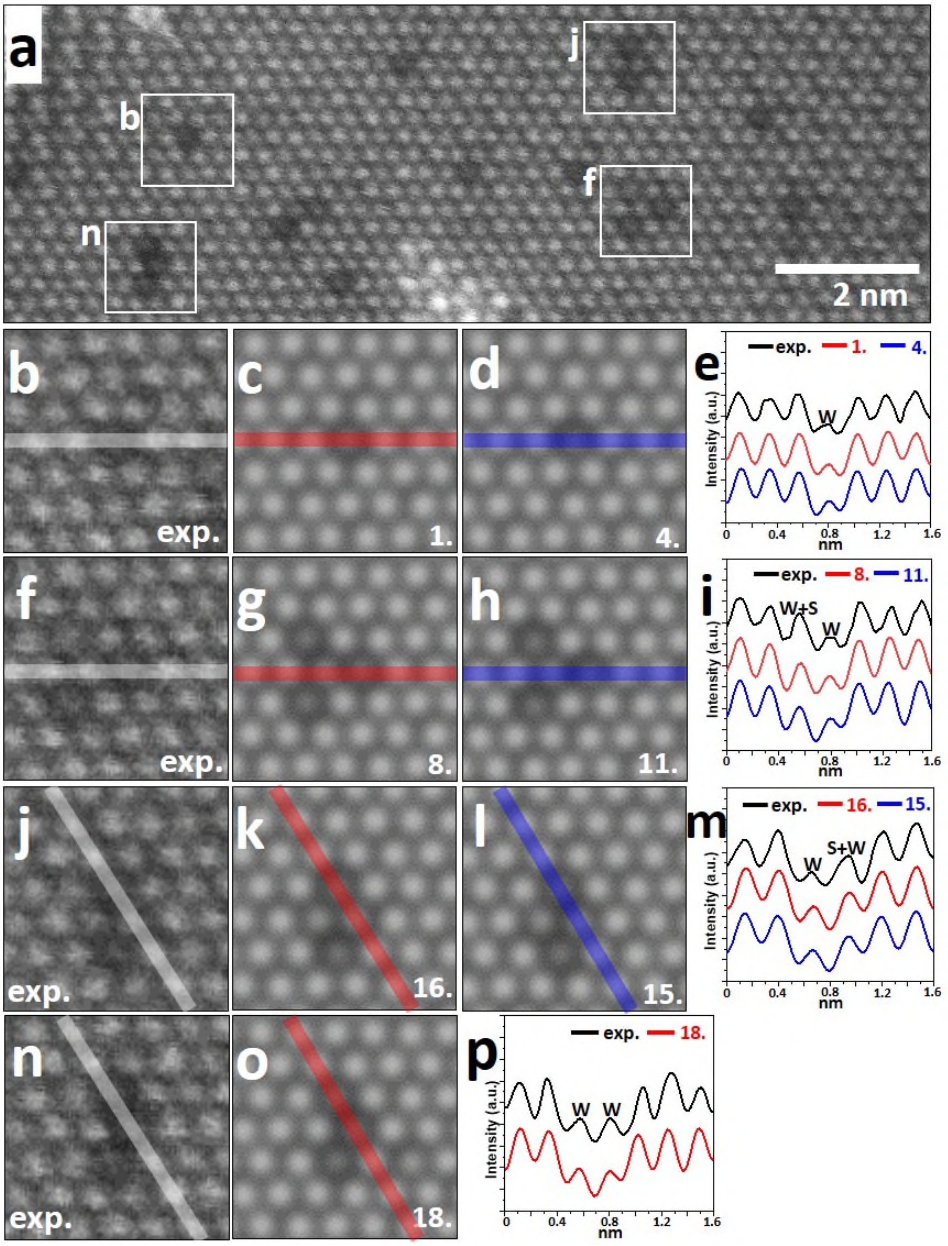

**Figure 3.** (a) ADF-STEM image showing the type of nanopores in 3R (ABC) stacked trilayer WS$_2$. (b, f, j, n) Magnified images of the white boxes in (a). (c,d) Multislice ADF-STEM image simulations corresponding to the atomic models in Figure S4(a) and (b). (e) Intensity line profiles measured from the selected white, red, and blue lines in (b), (c), and (d), respectively. (g) and (h) Multislice ADF-STEM image simulations corresponding to the atomic models in Figure S4(c) and (d). (i) Intensity line profiles measured from the selected white, red, and blue lines in (f), (g), and (h), respectively. (k) and (l) Multislice ADF-STEM image simulations corresponding to the atomic models in Figure S4(e) and (f). (i) Intensity line profiles measured from the selected white, red, and blue lines in (j), (k), and (l),

respectively. (o) Multislice ADF-STEM image simulation corresponding to the atomic model in Figure S4(g). (i) Intensity line profiles measured from the selected white and red lines in (n) and (o), respectively. The number in the simulated images indicates an order about the type of pores (see Figure S2 and S3 in supporting information).

Figure 4a shows a quadralayer $WS_2$ with the trilayer and bilayer $WS_2$. An inset of Figure 4a shows the whole multilayer $WS_2$ pyramid and a white box indicates Figure 4a. Figure 4b shows a magnified image taken from the region containing a yellow box in Figure 4a. Figure 4c shows a magnified image of the yellow box in Figure 4b and an intensity line profile measured from a yellow line in the Figure 4c. This line profile shows columns of this region marked by the yellow box have the same contrast level so that means this region is a 2H stacked bilayer. Figure 4d is a magnified image of a sky-blue box in Figure 4b. Figure 4e shows a multislice ADF image simulation corresponding to an atomic model in Figure 4f. Intensity line profiles across lines through the regions, indicated by white and red lines in Figure 4d and e, are measured for both experimental and simulated ADF images (Figure 4g). This region (Figure 4d) is the remaining trilayer after the top layer is etched. Therefore, unlike the trilayer described in Figure 2, atoms can be randomly missing in any layer or carbon contamination may be formed as this region is a defective trilayer. Thus, the intensity line profile of the region may not be relatively uniform. In the previous Figures, it has already turned out this trilayer region exhibits the 3R (ABC) stacking. Figure 4h shows a magnified image of a yellow-green box in Figure 4b. Figure 4i shows a multislice ADF image simulation corresponding to an atomic model in Figure 4j. Intensity line profiles across lines through the regions, indicated by white and red lines in Figure 4h and i, are measured for both experimental and simulated ADF images, showing a good agreement (Figure 4k). This quadralayer region exhibits the ABCC' stacking where 3R (ABC) and 2H (CC') stackings exist simultaneously. The lowest intensity of columns comes from overlapped $S_2$ and W atoms and the second comes from overlapped $S_2$, W, and $S_2$ atoms. The highest comes from overlapped W, $S_2$, and W atoms. About this quadralayer, we kept track of every stacking order to confirm this stacking order. So, when the top layer (C') is etched, the 3R (ABC) stacked trilayer is left (Figure 4d). And, when the two layers from the bottom layer are etched, the 2H (CC') stacked bilayer is left (Figure 4c) (see Figure S8). While the multilayer $WS_2$ sheets are being synthesized, they maintain a 1H phase, but different interlayer stacking orders can also be formed as shown in Figure 4. Also, depending on the etching direction, the visualization of the number of layers remaining after the etching is different because the interlayer stacking sequence is mixed.

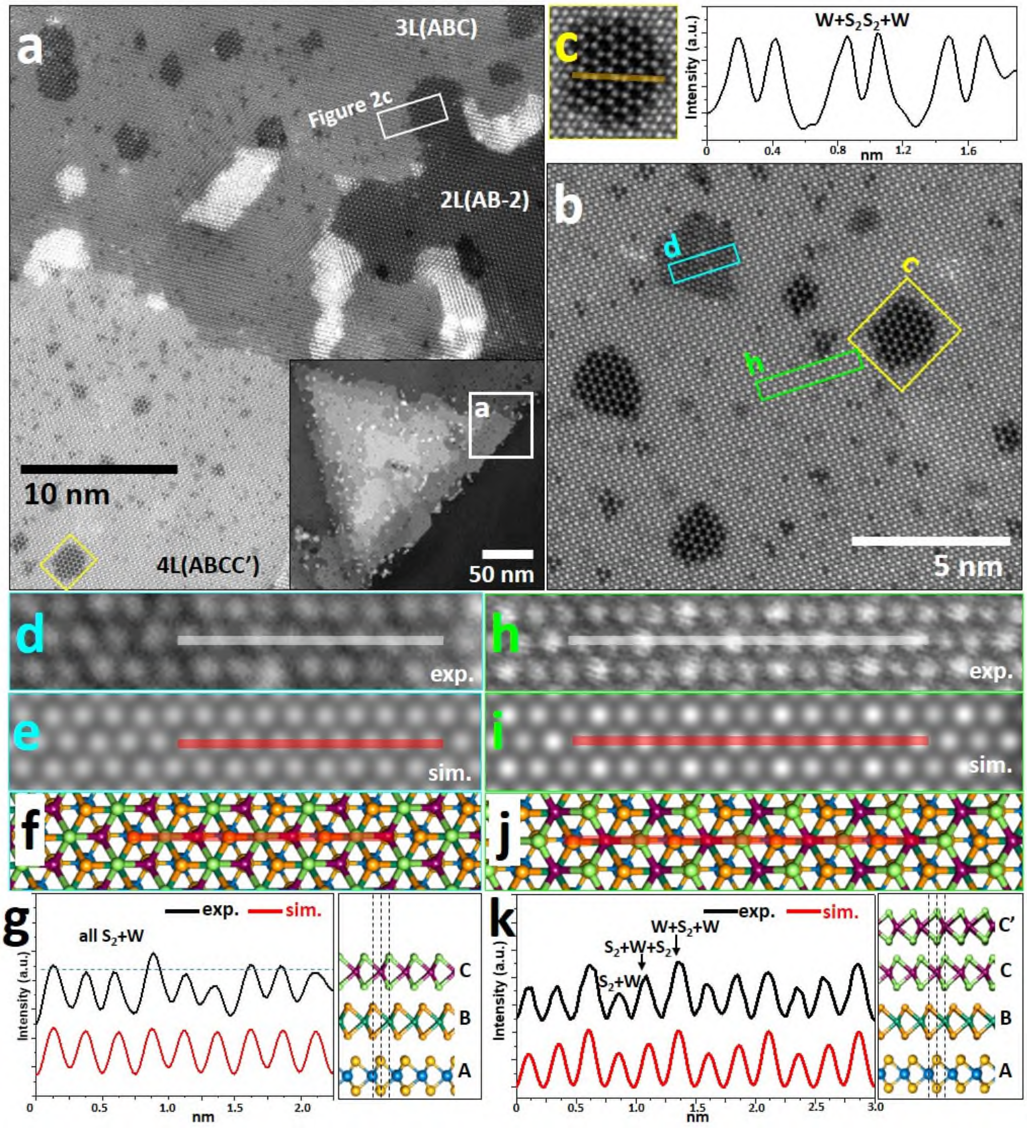

**Figure 4.** (a) ADF-STEM image showing the combined 3R and 2H (ABCC') stacked quadralayer WS$_2$ with the bilayer and trilayer. Inset in (a) shows the whole multilayer WS$_2$ pyramid and the white box in the inset indicates the (a). (b) Magnified image of the quadralayer containing the yellow box in (a). (c) Magnified image of the yellow box in (b) with the intensity line profile measured from the yellow line in (c). (d) Magnified image of the blue-sky box in (b) showing the ABC stacked trilayer. (e) Multislice ADF-STEM image simulation corresponding to the atomic model in (f). (f) Atomic model based on (d). (g) Intensity line profiles measured from the white and red lines in (d) and (e) with the side view of (f). (h) Magnified image of the blue-sky box in (b) showing the ABCC' stacked quadralayer. (i) Multislice ADF-STEM image simulation corresponding to the atomic model in (j). (j) Atomic model based on (h). (k) Intensity line profiles measured from the white and red lines in (d) and (e) with the side view of (j).

Figure 5a shows some nanopores which exist in the quadralayer $WS_2$. Figure 5b shows a magnified image of a white box labelled by b in Figure 5a. Figure 5c shows a multislice ADF-STEM image simulations corresponding to an atomic model in Figure 5d which structure is 2 S pairs and 1 W atom are missed in A ($V_{2S2,W}$ in A, Figure S6). Figure 5e shows an intensity line profile measured from a white line in Figure 5b has a good agreement with an intensity line profile measured from a red line in Figure 5c. Figure 5f is a magnified image of a white box labelled by f in Figure 5a. Figure 5g shows a multislice ADF-STEM image simulation corresponding to an atomic model in Figure 5h. This atomic structure is 3 S pairs and 1 W atom are missed in A ($V_{3S2,W}$ in A, Figure S6). Figure 5i shows an intensity line profile measured from a white line in Figure 5f has a good agreement with an intensity line profile measured from a red line in Figure 5g. Figure 5j is a magnified image of a white box labelled by j in Figure 5a. Figure 5k shows a multislice ADF-STEM image simulation corresponding to an atomic model in Figure 5l. The atomic structure of Figure 5k is 6 S pairs and 3 W atoms are missed in A, 1 W atom is missed in B, and 1 S atom is missed in C ($V_{6S2,3W}$ in A/$V_W$ in B/$V_S$ in C, Figure S6). Figure 5m shows an intensity line profile measured from a white line in Figure 5j has a good agreement with an intensity line profile measured from a red line in Figure 5k.

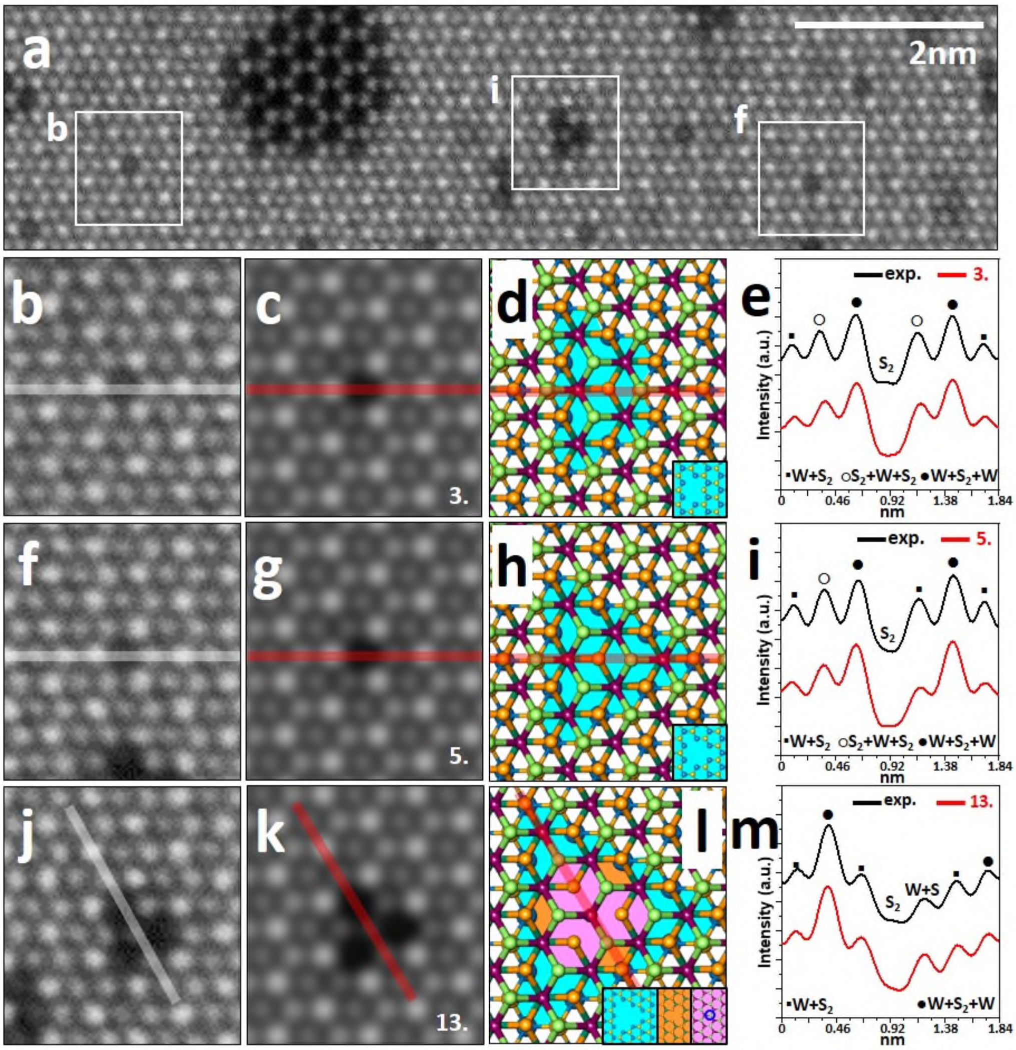

**Figure 5.** (a) ADF-STEM image showing the type of nanopores in combined 3R and 2H (ABCC') stacked quadralayer $WS_2$. (b, f, j) Magnified images of the white boxes in (a). (c, g, k) Multislice ADF-STEM image simulations corresponding to the atomic models in (d), (h), and (l). (d, h, l) Atomic models based on (b), (f), and (j), respectively. Insets indicate atomic structures in layers where pores exist. (e, i, m) Intensity line profiles measured from the selected white and red lines in (b) and (c), (f) and (g), (j) and (k), respectively. A, B, and C layers are coloured by sky-blue, orange, and pink, respectively. The number in the simulated images indicates an order about the type of pores (see Figures S6 and S7 in supporting information).

Figure 6a shows the entire multilayer region and an analysed region as shown in Figure 6b, indicated by a white box. Figure 6b shows a pentalayer $WS_2$ with the quadralayer $WS_2$. Figure

6c shows the magnified image of a yellow box in Figure 6b. Figure 6d shows a multislice ADF image simulation corresponding to an atomic model in Figure 6e. Intensity line profiles across lines through the regions, indicated by white and red lines in Figure 6c and d, are measured for both experimental and simulated ADF images, showing a good agreement (Figure 6f). In the Figure 4, it has already turned out this quadralayer region exhibits the combined 3R and 2H (ABCC') stacking. About the pentalayer, the upper layer was formed on the C' layer as the 3R stacking order. So, this region exhibits the ABCC'D' stacking order.

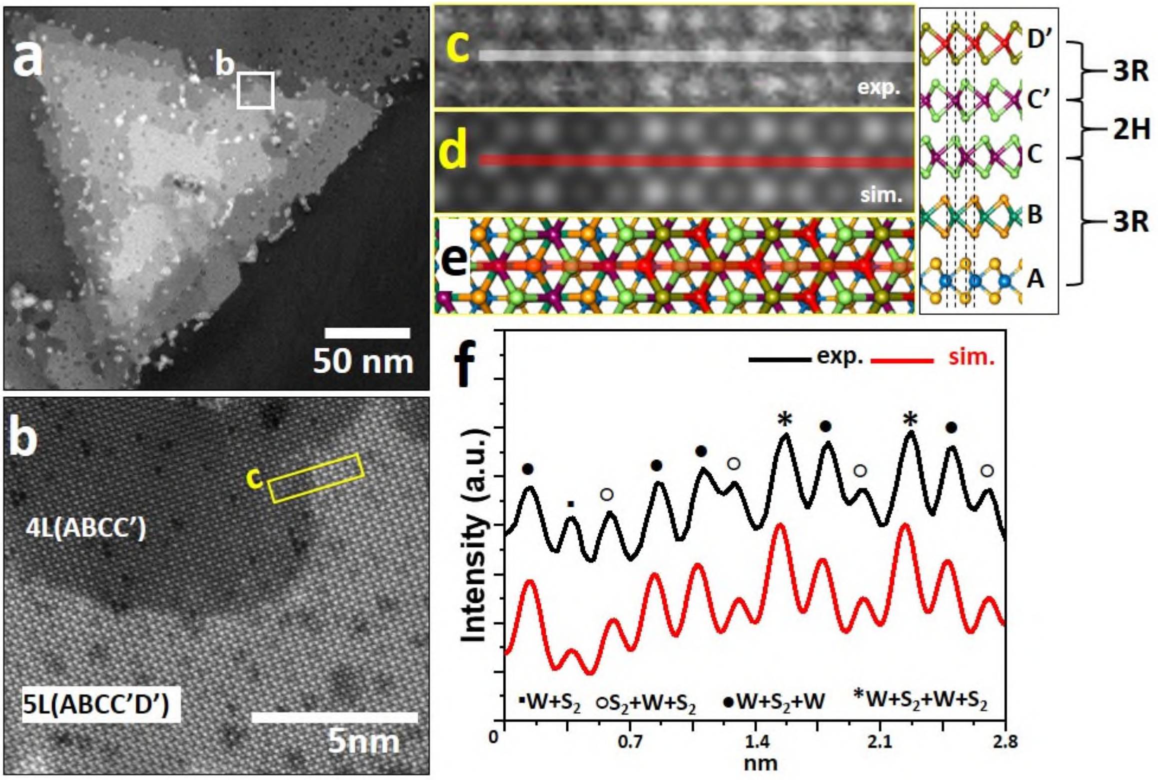

**Figure 6.** (a) ADF-STEM image showing the step edge configuration of ABCC'D' stacked pentalayer $WS_2$. (b) Magnified image of the white box in (a). (c) Magnified image of the yellow box in (b). (d) Multislice ADF-STEM image simulation corresponding to the atomic model of (e). (e) Atomic model with the side view. (f) Intensity line profiles measured from the white and red lines in (c) and (d).

In the case of spiral pyramids[29-32], all the layers have the same direction so inversion symmetry is broken due to the Burgers vector of the screw dislocation, which induces the spiral pyramid. On the other hand, an interfacial stacked structure is always a layered form step by step and it can be seen like the pyramid analysed by the low magnification TEM image as shown in Figure 1(a). Therefore, the mixed 2H/3R polytype can be seen in the pyramids formed by the interfacial nucleation, unlike the spiral.

Figure 7a shows a bilayer step edge configuration of 3R (AB-1) stacked bilayer $WS_2$. This region is considerably separated from the multilayer $WS_2$ pyramid region, which is continuously described in previous images. Monolayer (1L) and bilayer (2L) each have an obvious contrast difference as the contrast comes from the atom packing information along the Z-axis of the stacking order in mono- and bilayer $WS_2$. A particle having higher contrast is a W cluster, which stay attached to the local area.[33] Figure 7b shows the magnified image taken from the region marked with a white box in Figure 7a with the corresponding atomic model and a multislice ADF image simulation shown in Figure 7c and d, respectively. Intensity line profiles across lines through the bilayer $WS_2$ step edge, indicated by a white line in Figure 7b and a red line in Figure 7d, are measured for experimental image and simulated ADF image, showing a good agreement (Figure 7e). The ADF-STEM image indicates that this bilayer region exhibits 3R stacking. In the 3R stacked bilayer, ADF-STEM images look like this is significantly similar to monolayer (1H) $WS_2$ as the contrast of alternating atoms in hexagonal lattices are the higher than the others as shown in Figure 8a and 9a. But, the higher contrast atoms of the bilayer come from the overlapped W and $S_2$ atoms and the others come from the W atom.

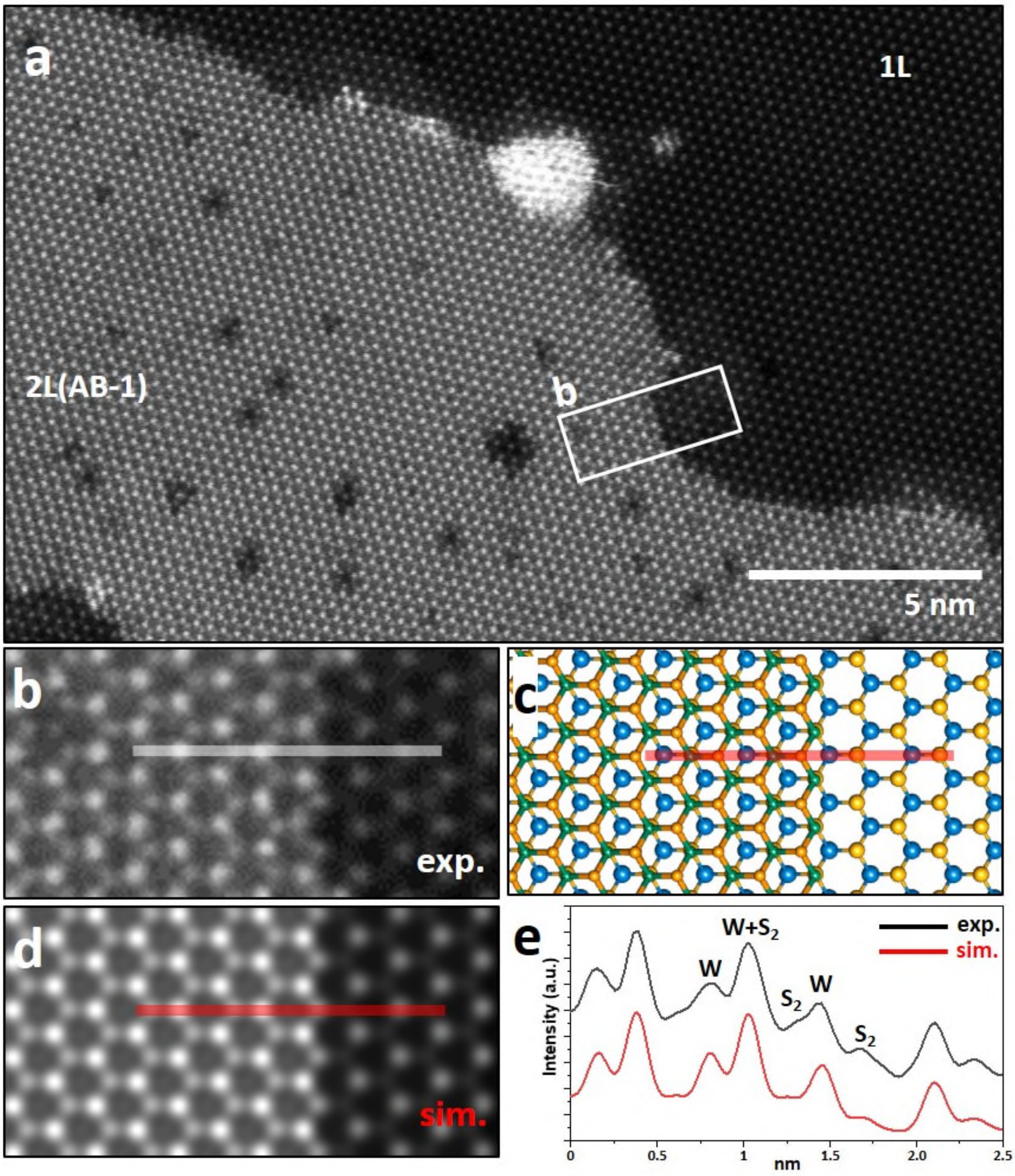

**Figure 7.** (a) ADF-STEM image the bilayer step edge configuration of 3R (AB-1) stacked bilayer WS$_2$. (b) Magnified image of the white box in (a). (c) Atomic model based on (b). (d) Multislice ADF-STEM image simulation corresponding to the atomic model in (c). (e) Intensity line profiles measured from the selected line (white and red lines) in (b) and (d), respectively. The structure corresponds to the line marked by the red line in (c).

Figure 8a and 9a show some defects such as vacancies and a substitutional dopant which exist in bilayer $WS_2$. Unlike the monolayer, it is likely that a variety of types of point defects can be observed depending on which layer the atoms are missed. So, the various detailed atomic structures can be simulated (see Figure S10 and S11). Among them, we focused on 4 types of the defects because they are frequently observed in the bilayer $WS_2$. Besides, since we have already figured out the stacking order of that, we could find out the detailed atomic structures of the pores. Figure 8b indicates a magnified image of a white box labelled by b in Figure 8a and Figure 8c shows a multislice ADF-STEM image simulation corresponding to an atomic model in Figure 8d. Based on previous research[34], this structure is a single Cr atom substituted at a W site in T-L (Cr @W in T-L, see Figure S10). About substitution of single Cr atom at W positions, our CVD grown monolayer $WS_2$ has been characterised in previous work using SEM, AFM, Raman, PL, EDX;[35] however, no evidence of Cr dopants was detected. However, the possibility that Cr atoms, which were present as impurity particles, acted as the substitution at the position of metal atoms in TMDs was clearly reported in our previous paper.[35] ADF-STEM imaging of the CVD prepared $WS_2$ revealed considerable low contrast atoms situated on the W site, which are distinct from low contrast features located on the S site.[33] An intensity line profile measured from a white line in Figure 8b has a good agreement with an intensity line profile measured from a red line in Figure 8c. Figure 8f is a magnified image of a white box labelled by f in Figure 8a. This structure is a vacancy where 3 S pairs and 1 W atom are missed in T-L ($V_{3S2,\ W}$ in T-L, see Figure S10). Figure 8g shows a multislice ADF-STEM image simulation corresponding to an atomic model in Figure 8h. An intensity line profile measured from a white line in Figure 8f has a good agreement with an intensity line profile measured from a red line in Figure 8g. Figure 8j is a magnified image of a white box labelled by j in Figure 8a. This structure is where 3 S pairs are missed in T-L and 1 W atom is missed in B-L ($V_{3S2}$ in T-L/$V_W$ in B-L, see Figure S10). Figure 8k shows a multislice ADF-STEM image simulation corresponding to an atomic model in Figure 8l. An intensity line profile measured from a white line in Figure 8j has a good agreement with an intensity line profile measured from a red line in Figure 8k.

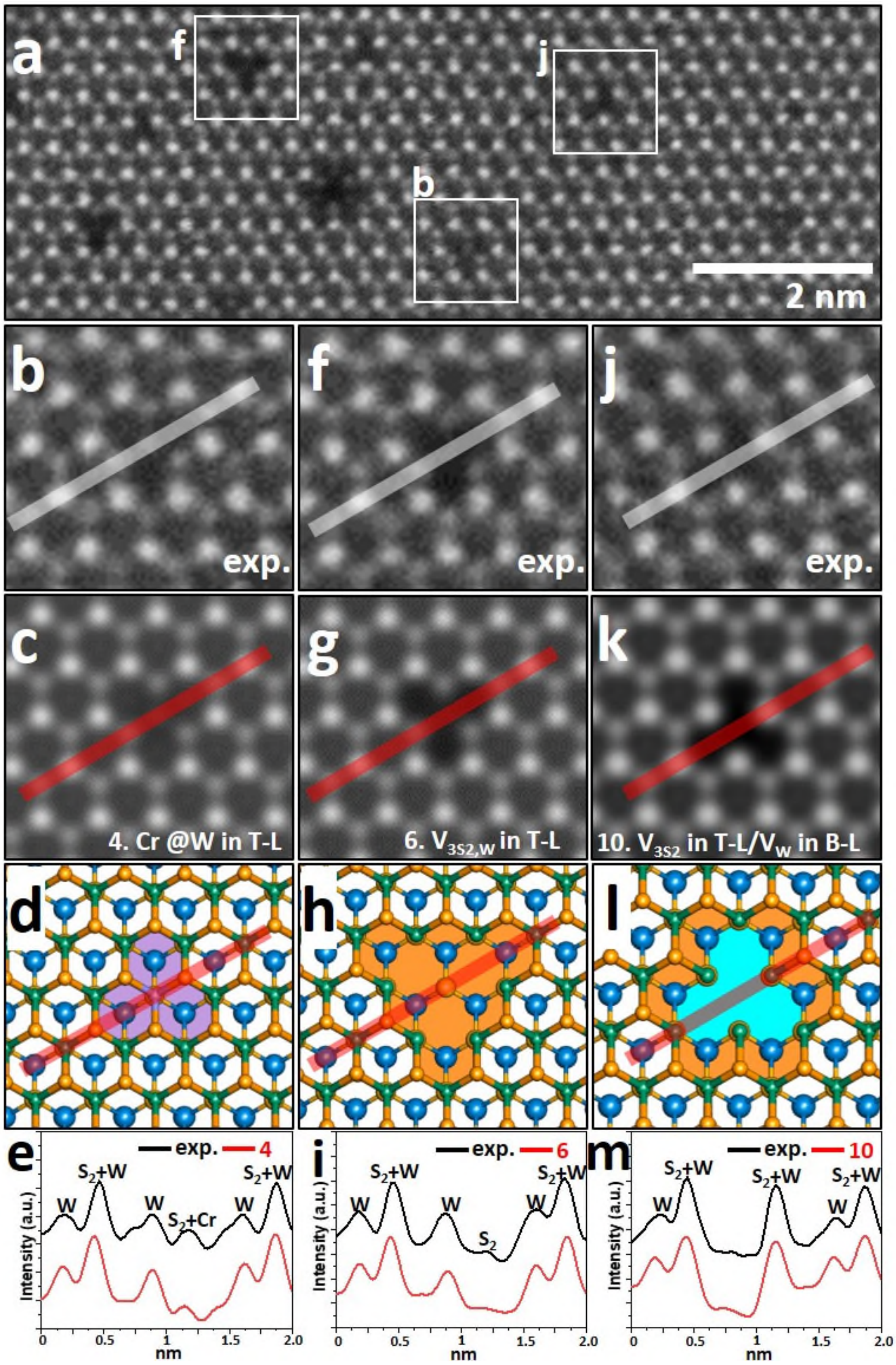

**Figure 8.** (a) ADF-STEM image showing the type of nanopores in 3R (AB-1) stacked bilayer $WS_2$. (b, f, j) Magnified images of the white boxes in (a). (c, g, k) Multislice ADF-STEM image simulations corresponding to the atomic models in (d), (h), and (l), respectively (see Figure S10 in supporting information). (e, i, m) Intensity line profiles measured from the selected lines (white and red lines) in

(b) and (c), (f) and (g), (j) and (k), respectively. The structure corresponds to the lines marked by the red line in the atomic models.

Interestingly, we observed a snowflake shaped pore in the 3R (AB-1) stacked bilayer as shown in Figure 9a. Figure 9b is a magnified image of a white box in Figure 9a and Figure 9c is a well-matched multislice ADF-STEM image simulation corresponding to an atomic model in Figure 9f with the experimental image. This structure is where 3 W atoms and 1 S pairs are missed in T-L ($V_{3W,S2}$ in T-L, see Figure S10). Figure 9d shows a quite similar structure to Figure 9b, which structure is that 1 S pair is missed in T-L and 6 S pairs and 3 W atoms are missed in B-L ($V_{S2}$ in T-L/$V_{6S2,3W}$ in B-L, see Figure S10). The difference between both is higher contrast site of atoms positioned in the middle of Figure 9c and d; For Figure 9c, the higher intensity of three atoms located at the middle comes from three W atoms in B-L (three blue spheres positioned at the middle of the atomic model in Figure 9f while, in the case of Figure 9d, the higher intensity of three atoms located at the middle comes from three W atoms in T-L (three green spheres positioned ate the middle of the atomic model in Figure 9g). Therefore, considering only 3 atoms positioned at the middle between Figure 9c and d, they each have an opposite orientation. The number in the simulated images indicates an order about the type of pores (see Figures S10 and S11 in supporting information).

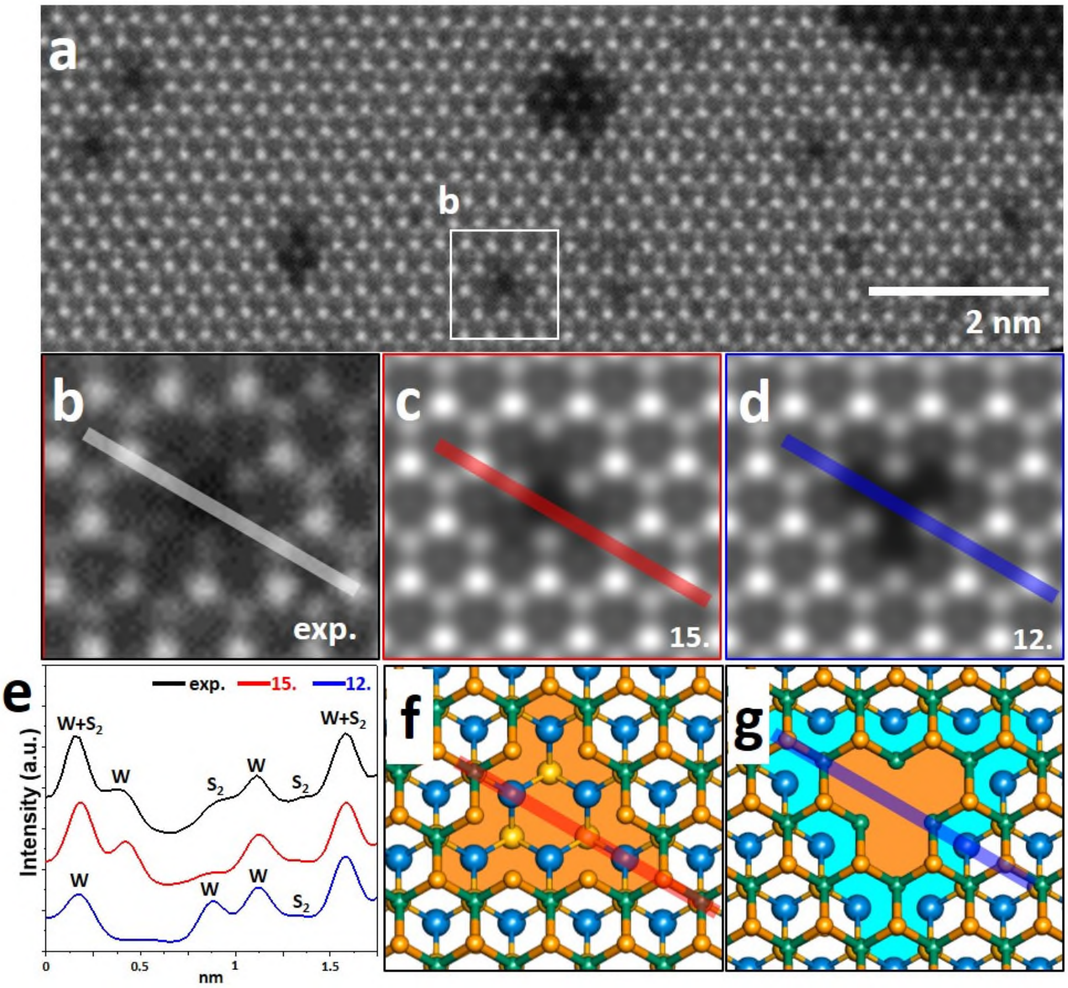

**Figure 9.** (a) ADF-STEM image showing snowflake shaped pores in bilayer 3R (AB-1) stacked $WS_2$. (b) Magnified image of the white box in (a). (c) Multislice ADF-STEM image simulation corresponding to the atomic model in (f). (f) Atomic model based on (b). (d) Multislice ADF-STEM image simulation corresponding to the atomic model in (g). The higher intensity of three atoms located in the middle of (c) and (d) comes from three W atoms located in the middle of (f) (three blue spheres in bottom-layer) and (a) (three green spheres in top-layer), respectively. (e) Intensity line profiles measured from white, red, and blue lines in (b-d). The number in the simulated images indicates an order about the type of pores (see Figures S10 and S11 in supporting information).

## Conclusion

By using ADF-STEM imaging and multislice image simulation, we show how the stacking order and defect types in multilayer $WS_2$ are quantified at the atomic scale. Until the pentalayer, we kept tracking of their stacking orders everything one by one individually and then analysed atomic structures of the pores existing in each layer. Besides, as the number of layers increases, the number of pore types that can exist in each layer increases, so these were summarized as the catalogue in supporting information. These defects are considered to be intrinsic defects formed by an oxidation and a high temperature rather than by engineered defects caused by an electron beam, and it is seen that material aging occurs in both directions because the layer in which defects exist is not uniform. Until the trilayer, their stacking orders are only 3R but, at the quadralayer, it has combined 3R and 2H stacking order like as ABCC' even though the multilayer $WS_2$ was synthesised under the same condition. In addition, this stacking order changes again by being synthesized another top layer on the quadralayer with the 3R stacking order. This work shows that multilayer TMDs composed of 1H phase can have the combined 3R and 2H stacked order by different interlayer stacking order, and this work's detailed quantification and confirmation of the stacking order and existing nanopores will suggest understanding atomic structural behavior of multilayer TMDs.

## Methods

*Multilayer $WS_2$ pyramids Chemical Vapour Deposition Synthesis and Transfer.* $WS_2$ multilayers were grown using CVD, based on a previously reported method.[35] A double-walled quartz tube was inserted through two tube furnaces. S precursor powder (300 mg, 99.5%) was placed in the outer tube and aligned with the first furnace. $WO_3$ (200 mg, 99.9%) precursor was inserted into the inner tube within the second CVD tube furnace, at the centre of the hot-zone of the furnace, and the substrate ($Si/SiO_2$ chip) was located in the outer tube with a precalibrated distance further downstream. Ar carrier gas was used to bring reactant vapor to the substrate, permitting $WO_3$ sulfurization at the substrate. The first, S-containing, furnace was held at 180 °C, and the second furnace at 1170 °C, with the reaction stage taking 3 min. Samples were rapidly cooled by removal from the furnace following the reaction stage.

Transfer was achieved by spin-coating the sample with a supporting poly (methyl acrylate) (PMMA) scaffold (8% wt, Mw 495k). The PMMA/$WS_2$ stack was separated from the $SiO_2$/Si substrate by KOH etching (1 M) at 60 °C. The PMMA/$WS_2$ film was transferred via clean glass slides to deionized water to rinse residue from the $WS_2$ side, which was repeated several times. The film was then transferred to the sample chip, allowed to dry overnight, and then heated on a hot plate at 150 °C to drive off remaining water and promote sample adhesion.

*Transmission Electron Microscopy with an in Situ Heating Holder.* ADF-STEM was conducted using an aberration-corrected JEOL ARM300CF STEM equipped with a JEOL ETA corrector operated at an accelerating voltage of 60 kV located in the electron Physical Sciences Imaging Centre (ePSIC) at Diamond Light Source. Dwell times of 5−20 µs and a pixel size of 0.006 nm $px^{-1}$ was used for imaging with a convergence semi-angle of 31.5 mrad, a beam current of 44 pA, and inner-outer acquisition angles of 49.5−198 mrad.

Temperature dependent ADF-STEM imaging up to 1000°C was performed using a commercially available *in situ* heating holder from DENS Solutions (SH30-4M-FS). FIB was used to cut open slits in the $Si_3N_4$ membrane to enable suspended $WS_2$ samples for imaging. Heating the sample was achieved by passing a current through a platinum resistive coil embedded in the TEM chip (DENS Solutions DENS-C-30). The resistance of the platinum coil was monitored in a four-point configuration, and the temperature was calculated using the Callendar-Van Dusen equation (with calibration constants provided by the manufacturer). Slits were fabricated in the $Si_3N_4$ membranes using focused ion beam milling before transferring the $WS_2$.

*Image Processing and Simulation.* ImageJ was used to process the ADF images. Multislice image simulations for ADF images were performed using the multislice method implemented in the JEMS software. Parameters for image simulations were based on the experimental condition of the JEOL ARM300CF. The chromatic aberration at 60 kV is 0.89 mm with an energy spread of 0.42 eV. The probe size is 65 pm and the convergence semi-angle is 31.5 mrad. The angle range for dark field imaging is from 49.5 mrad to 198 mrad. Spherical aberration is 5 μm.

**Supporting information.** Catalogues about atomic structures of defects.

## ACKNOWLEDGMENT

JHW thanks the support from the Royal Society and the ERC Consolidator grant (725258 CoG 2016 LATO). We thank Diamond Light Source for access and support in use of the electron Physical Science Imaging Centre (EM16854) that contributed to the results presented here.

## REFERENCES

1. Splendiani, A.; Sun, L.; Zhang, Yuanbo.; Li, Tianshu.; Kim, J.; Chim, C.-Y.; Galli, G.; Wang, F. Emerging Photoluminescence in Monolayer $MoS_2$. *Nano Lett.* **2010**. *10*, 1271–1275.
2. Xiao, D.; Liu, G.-B.; Feng, W.; Xu, X.; Yao, W. Coupled Spin and Valley Physics in Monolayers of $MoS_2$ and Other Group-VI Dichalcogenides. *Phys. Rev. Lett.* **2012**. *108*, 196802.
3. Chhowalla, M.; Shin, H.S.; Eda, G.; Li, L.-J.; Loh, K.P.; Zhang, H. The Chemistry of Two-Dimensional Layered Transition Metal Dichalcogenide Nanosheets. *Nat. Chem.* **2013**. *5*, 263–275.
4. Voiry, D.; Mohite, A.; Chhowalla, M. Phase Engineering of Transition Metal Dichalcogenides. *Chem. Soc. Rev.* **2015**. *44*, 2702–2712.

5. Kan, M.; Wang, J.Y.; Li, X.W.; Zhang, S.H.; Li, Y.W.; Kawazoe, Y.; Sun, Q.; Jena, P. Structures and Phase Transition of a $MoS_2$ Monolayer. *J. Phys. Chem. C* **2014**. *118*, 1515–1522.
6. Leng, K.; Chen, Z.; Zhao, X.; Tang, W.; Tian, B.; Nai, C.T.; Zhou, W.; Loh, K. P. Phase Restructuring in Transition Metal Dichalcogenides for Highly Stable Energy Storage. *ACS Nano* **2016**, *10*, 9208–9215.
7. Kappera, R.; Voiry, D.; Yalcin, S. E.; Branch, B.; Gupta, G.; Mohite, A. D.; Chhowalla, M. Phase-Engineered Low-Resistance Contacts for Ultrathin $MoS_2$ Transistors. *Nat. Mater.* **2014**, *13*, 1128–1134.
8. Enyashin, A. N.; Yadgarov, L.; Houben, L.; Popov, I.; Weidenbach, M.; Tenne, R.; Bar-Sadan, M.; Seifert, G. New Route for Stabilization of 1T-WS2 and $MoS_2$ Phases. *J. Phys. Chem. C* **2011**, *115*, 24586–24591.
9. Calandra, M. Chemically Exfoliated Single-Layer $MoS_2$: Stability, Lattice Dynamics, and Catalytic Adsorption from First Principles. *Phys. Rev. B* **2013**, *88*, 245428.
10. Wang, S.; Sawada, H.; Allen, C. S.; Kirkland, A. I.; Warner, J. H. Orientation Dependent Interlayer Stacking Structure in Bilayer $MoS_2$ Domains. *Nanoscale* **2017**, *9*, 13060–13068.
11. Zhao, X.; Ning, S.; Fu, W.; Pennycook, S. J.; Loh, K. P. Differentiating Polymorphs in Molybdenum Disulfide via Electron Microscopy. *Adv. Mater.* **2018**, 1802397.
12. Zhou, S.; Wang, S.; Li, H.; Xu, W.; Gong, C.; Grossman, J. C.; Warner, J. H. Atomic Structure and Dynamics of Defects in 2D $MoS_2$ Bilayers. *ACS Omega* **2017**, *2*, 3315–3324.
13. Zhou, S.; Wang, S.; Shi, Z.; Sawada, H.; Kirkland, A. I.; Li, L.; Warner, J. H. Atomically Sharp Interlayer Stacking Shifts at Anti-Phase Grain Boundaries in Overlapping $MoS_2$ Secondary Layers. *Nanoscale* **2018**, *10*, 16692–16702.

14. Wang, S.; Li, H.; Sawada, H.; Allen, C. S.; Kirkland, A. I.; Grossman, J. C.; Warner, J. H. Atomic Structure and Formation Mechanism of Sub-Nanometer Pores in 2D Monolayer $MoS_2$. *Nanoscale* **2017**, *9*, 6417−6426.

15. Yoshimura, A.; Lamparski, M.; Kharche, N.; Meunier, V. First Principles Simulation of Local Response in Transition Metal Dichalcogenides under Electron Irradiation. *Nanoscale* **2018**, *10*, 2388−2397.

16. Komsa, H.-P.; Kurasch, S.; Lehtinen, O.; Kaiser, U.; Krasheninnikov, A. V. From Point to Extended Defects in Two Dimensional $MoS_2$: Evolution of Atomic Structure under Electron Irradiation. *Phys. Rev. B: Condens. Matter Mater. Phys.* **2013**, *88*, 035301.

17. Wang, S.; Lee, G.-D.; Lee, S.; Yoon, E.; Warner, J. H. Detailed Atomic Reconstruction of Extended Line Defects in Monolayer $MoS_2$. *ACS Nano* **2016**, *10*, 5419−5430.

18. Ryu, G.H.; Lee, J.; Kim, N.Y.; Lee, Y.; Kim, Y.; Kim, M. J.; Lee, C.; Lee, Z. Line-Defect Mediated Formation of Hole and Mo clusters in Monolayer Molybdenum Disulfide. *2D Mater.* **2016**, 3, 014002.

19. Chen, Q.; Li, H.; Zhou, S.; Xu, W.; Chen, J.; Sawada, H.; Allen, C. S.; Kirkland, A. I.; Grossman, J. C.; Warner, J. H. Ultralong 1D Vacancy Channels for Rapid Atomic Migration During 2D Void Formation in Monolayer $MoS_2$. *ACS Nano* **2018**, *12*, 7721−7730.

20. Zan, R.; Ramasse, Q. M.; Jalil, R.; Georgiou, T.; Bangert, U.; Novoselov, K. S. Control of Radiation Damage in $MoS_2$ by Graphene Encapsulation. *ACS Nano* **2013**, *7*, 10167-10174.

21. Algara-Siller, G.; Kurasch, S.; Sedighi, M.; Lehtinen, O.; Kaiser, U. The Pristine Atomic Structure of $MoS_2$ Monolayer Protected from Electron Radiation Damage by Graphene. *Appl. Phys. Lett.* **2013**, *103*, 203107.

22. Wu, R. J.; Odlyzko, M.L.; Mkhoyan, K. A. Determining the thickness of atomically thin $MoS_2$ and $WS_2$ in the TEM. *Ultramicroscopy* **2014**, *147*, 8–20.
23. Constantinescu, G.; Kuc, A.; Heine, T. Stacking in Bulk and Bilayer Hexagonal Boron Nitride. *Phys. Rev. Lett.* **2013**, *111*, 036104.
24. van der Zande, A. M.; Huang, P. Y.; Chenet, D.A.; Berkelbach, T. C.; You, Y.; Lee, G.-H.; Heinz, T.F.; Reichman, D. R.; Muller, D. A.; Hone, J. C. Grains and Grain Boundaries in Highly Crystalline Monolayer Molybdenum Disulphide. *Nat. Mater.* **2013**, *12*, 554–561.
25. Yan, J.; Xia, J.; Wang, X.; Liu, L.; Kuo, J.-L.; Tay, B. K.; Chen, S.; Zhou, W.; Liu, Z.; Shen, Z. X. Stacking-Dependent Interlayer Coupling in Trilayer $MoS_2$ with Broken Inversion Symmetry. *Nano Lett.* **2015**, *15*, 8155−8161.
26. Xia, J.; Yan, J.; Shen, Z. X. Transition Metal Dichalcogenides: Structural, Optical and Electronic Property Tuning via Thickness and Stacking. *FlatChem* **2017**, *4*, 1−19.
27. Puretzky, A. A.; Liang, L.; Li, X.; Xiao, K.; Wang, K.; Mahjouri-Samani, M.; Basile, L.; Idrobo, J. C.; Sumpter, B. G.; Meunier, V.; Geohegan, D. B. Low-Frequency Raman Fingerprints of Two-Dimensional Metal Dichalcogenide Layer Stacking Configurations. *ACS Nano* **2015**, *9*, 6333−6342.
28. L, J.-U.; Kim, K.; Han, S.; Ryu, G.H.; Lee, Z.; Cheong, H. Raman Signatures of Polytypism in Molybdenum Disulfide. *ACS Nano* **2016**, *10*, 1948–1953.
29. Ly, T. H.; Zhao, J.; Kim, H.; Han, G.H.; Nam, H.; Lee, Y.H. Vertically Conductive $MoS_2$ Spiral Pyramid. *Adv. Mater.* **2016**, *28*, 7723-7728.
30. Sarma, P. V.; Patil, P. D.; Barman, P. K.; Kini, R. N.; Shaijumon, M. M. Controllable Growth of Few-Layer Spiral $WS_2$. *RSC Adv*. **2016**, *6*, 376.

31. Zhang, L.; Liu, K.; Wong, A. B.; Kim, J.; Hong, X.; Liu, C.; Cao, T.; Louie, S. G.; Wang, F.; Yang, P. Three-Dimensional Spirals of Atomic Layered $MoS_2$. *Nano Lett.* **2014**, *14*, 6418-6423.
32. Tay, R. Y.; Park, H.J.; Lin, J.; Ng, Z. K.; Jing, L.; Li, H.; Zhu, M.; Tsang, S. H.; Lee, Z.; Teo, E. H. T. Concentric and Spiral Few-Layer Graphene: Growth Driven by Interfacial Nucleation vs Screw Dislocation. *Chem. Mater*. **2018**, *30*, 6858-6866.
33. Ryu, G.H.; France-Lanord, A.; Wen, Y.; Zhou, S.; Grossman, J. C.; Warner, J. H. Atomic Structure and Dynamics of Self Limiting Sub-Nanometer Pores in Monolayer $WS_2$. ACS Nano 2018 12, 11638-11647.
34. Robertson, A. W.; Lin, Y.-U.; Wang, S.; Sawada, H.; Allen, C. S.; Chen, Q.; Lee, S.; Lee, G.-D.; Lee, J.; Han, S.; Yoon, E.; Kirkland, A. I.; Kim, H.; Suenaga, K.; Warner, J. H. Atomic Structure and Spectroscopy of Single Metal (Cr, V) Substitutional Dopants in Monolayer $MoS_2$. *ACS Nano* **2016**, *10*, 10227-10236.
35. Rong, Y.; Fan, Y.; Koh, A. L.; Robertson, A. W.; He, K.; Wang, S.; Tan, H.; Sinclair, R.; Warner, J. H. Controlling Sulphur Precursor Addition for Large Single Crystals Domains of $WS_2$. *Nanoscale* **2014**, *6*, 12096−12103.